Journal of Membrane Science & Research

journal homepage: www.msrjournal.com

Research Paper

# Hybrid Nanofiltration–Distillation Process for Ultrapure Isopropyl Alcohol: Experimental Validation and PRO-II Simulation for Semiconductor Applications

Dileep Kumar Fothedar [1, 2, 3], Nivedita Sahu [1, 2], Namita Roy Choudhury [3], Sundergopal Sridhar [1, 2, *]

[1] *Membrane Separations Group, Process Engineering, and Technology Transfer, CSIR-Indian Institute of Chemical Technology, Tarnaka, Hyderabad-500007, Telangana, India*
[2] *Academy of Scientific and Innovative Research (AcSIR), Ghaziabad-201002, India*
[3] *Chemical and Environmental Engineering, School of Engineering, Royal Melbourne Institute of Technology (RMIT), Melbourne, VIC 3001, Australia*

## Article info

Received 2025-10-19
Revised 2026-0-04
Accepted 2026-02-10
Available online 2026-02-10

## Keywords

Electronic Grade
Metal Ions
Nanofiltration
Rejection
High Purity
ICP-OES

## Highlights

- A hybrid nanofiltration–distillation system was developed for ultrapure isopropyl alcohol purification.
- The HF-NF-300AR membrane achieved >98.2% rejection with flux values of 180–220 L/m2.h.
- PRO-II simulation optimized process conditions at 15 bar and 15 modules for best performance.
- The product unit cost ranged between 126–157 $/m³, confirming industrial-scale feasibility.
- The hybrid process offers a sustainable, energy-efficient route for semiconductor-grade IPA production.

## Graphical abstract

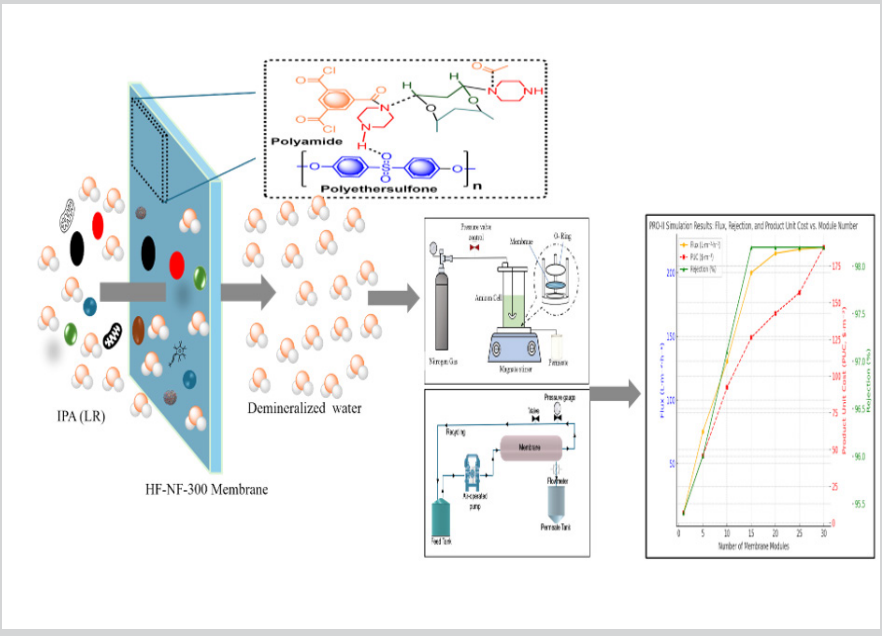


## Abstract

Isopropyl alcohol (IPA) is widely used as a cleaning and processing solvent in semiconductor manufacturing, where trace impurities can severely impact device performance. Conventional purification methods, such as distillation, are energy-intensive and costly, driving the need for sustainable alternatives. In this study, a membrane-integrated purification approach was developed to upgrade laboratory reagent-grade (LR) IPA to ultrapure quality. A hydrophilic nanofiltration (HF-NF-300) membrane was fabricated via interfacial polymerization and evaluated in an Amicon stirred cell, a pilot-scale membrane module, and a vacuum distillation unit. Bench-scale experiments achieved a flux of 1.25–4.11 L/m².h and metal ion rejection exceeding 91.9%. Pilot-scale trials confirmed scalability, delivering stable performance with a flux of 1.32–3.01 L/m².h and a recovery of ~44%. Hybrid operation combining NF membranes with vacuum distillation further enhanced purification, achieving an average metal-ion rejection of ~97.3% and near-complete (>99%) removal of Ca, Na, Cr, and Mg. Process modelling using PRO-II™ simulations identified the optimal operating condition at 10–15 bar using 10–25 modules (of 2.5 m² area per module), for achieving a flux of 180–220 L/m².h, rejection (>97%), and product unit cost (126–157 $/m³). The results demonstrate that membrane-based IPA purification, combined with distillation polishing, provides a cost-effective, scalable route to producing ultrapure solvents for semiconductor and pharmaceutical applications.

© 2026 FIMTEC & MPRL. All rights reserved.

* Corresponding author: Sridhar11in@yahoo.com (S. Sridhar)

**DOI:** 10.22079/jmsr.2026.2075119.1732

## 1. Introduction

Organic solvents play a critical role in semiconductor manufacturing, particularly in wafer cleaning, lithography, development, and photoresist removal processes[1]. The use of ultrapure solvents is essential to minimize surface contamination and defect formation, which directly affect device performance and yield [2]. Even trace-level impurities in solvents, at concentrations as low as tens of parts per billion, can result in metal contamination on silicon wafers and lead to critical device failures [3]. Recent studies indicate that organic and metallic contaminants in isopropyl alcohol (IPA) used for wafer drying must be reduced from ~50 ppb to below 10 ppb to meet next-generation semiconductor requirements[4], [5]. Consequently, advanced purification techniques, such as membrane-based separations and ion-exchange processes, are increasingly employed to remove water, particulates, and ionic species from organic solvents and to comply with stringent semiconductor purity standards[6].

The development of cost-effective purification technologies for isopropyl alcohol (IPA) is essential in semiconductor manufacturing, where extremely high purity standards must be met. Large volumes of waste IPA are generated in semiconductor fabs, and conventional disposal methods such as incineration are both energy-intensive and environmentally unfavorable. Consequently, efficient recycling and purification strategies are critical for improving sustainability and reducing operational costs. Resin-based ultrapure systems have demonstrated the ability to reduce ionic impurities to sub-ppb levels suitable for semiconductor processes[7]. In parallel, advances in alternative solvents, improved drying technologies, and optimized process integration have contributed to reduced solvent consumption and enhanced cleaning efficiency [6], [8]. Collectively, these developments highlight the importance of advanced purification and recycling methods to meet stringent purity requirements while supporting sustainable semiconductor manufacturing.

Purification of isopropyl alcohol (IPA) for semiconductor applications is challenging due to stringent purity requirements and the complex nature of waste solvent streams. Achieving sub-part-per-billion (ppb) removal of ionic impurities is essential to prevent contamination during device fabrication. Resin-based ultrapure systems have demonstrated the ability to achieve such high purity levels through ion-exchange mechanisms in non-polar solvents; however, their scalability and long-term operational stability remain limiting factors[9]. Conventional distillation is further complicated by azeotrope formation in IPA–water systems, often requiring heteroazeotropic distillation with entrainers such as cyclohexane, which increases energy consumption and process complexity [10]. Although integrating renewable energy sources into distillation has been explored to reduce environmental impact, high capital costs and system integration challenges continue to limit widespread adoption[11]. Consequently, the need for energy-efficient, scalable, and reliable purification technologies continues to drive research in this area.

The durability of polymeric membranes in organic solvents remains a key challenge, as prolonged exposure can cause structural degradation and performance loss [6],[8]. This has driven research toward solvent-stable nanofiltration membranes that maintain integrity under harsh operating conditions[9]. In addition to chemical stability, achieving high selectivity in organic solvent nanofiltration (OSN) is critical, as it directly determines separation efficiency. However, limited understanding of solvent–solute transport mechanisms within OSN membranes continues to constrain predictive modelling and process optimization[12]. For semiconductor applications, stringent particle control in process chemicals is also essential, as particulate contamination can induce defects in sub-10 nm technology nodes [13]. Recent advances in hybrid and inorganic membrane materials, including metal–organic and covalent organic frameworks, show promise in improving membrane stability and selectivity in organic media[8].

Process simulation has emerged as a powerful tool for the design and optimization of hybrid membrane–distillation systems, enabling rigorous evaluation of mass balance, energy demand, and economic performance under industrial operating conditions. The integration of experimentally derived membrane transport parameters into commercial simulators enables reliable scale-up analysis and the identification of optimal operating windows, which remain insufficiently explored for ultrapure IPA purification.

The present study develops and evaluates a hybrid nanofiltration–distillation process for upgrading laboratory-grade IPA to ultrapure quality. A hydrophilic thin-film composite nanofiltration membrane was fabricated and systematically investigated at bench scale and pilot scale for trace metal ion removal. The membrane-treated IPA was further polished using vacuum distillation to enhance purity. In addition, a customized membrane model was implemented in PRO-II™ simulation software to assess process scalability, optimize operating conditions, and estimate product unit cost. The combined experimental and simulation-based approach provides a comprehensive framework for developing an energy-efficient, scalable, and industrially viable process for producing ultrapure IPA for semiconductor and high-value chemical applications.

## 2. Materials and Methods

### *2.1. Materials*

Polyethersulfone (PES) was procured from Solvay, Vadodara, India, to synthesize an ultra-porous substrate. Dimethyl formamide (DMF), IPA LR grade, and HCl were purchased from Sigma-Aldrich, Hyderabad, India. Hexane, trimesoyl chloride (TMC), and piperazine (PIP), cleaning chemicals like citric acid (CA), sodium hydroxide (NaOH), sodium metabisulfite (SMBS), and ethylenediaminetetraacetic acid (EDTA) were obtained from S.D. Fine Chemicals, Mumbai, India for the synthesis of flat sheet nanofiltration (NF) Polyamide (PA) membrane (HF-NF 300 AR) by interfacial polymerization technique. Hardware items such as pressure gauges, valves, tubing, connectors, elbows, skids, etc. An Amicon stirred cell was purchased from Merck Millipore, Sanath Nagar, Hyderabad, India, whereas the 1 L capacity dead-end stainless steel cell was fabricated with the help of workshop staff at IICT. A compressor is used to apply the pressure procured from RVR Enterprises, Hyderabad, Telangana. All glassware used in the study, including conical flasks, measuring cylinders, and sample collectors, was obtained from Borosil, Hyderabad, India, for sample preparation, experimentation, and analysis. Sumair Industries, Hyderabad, India. Pure water used in experimental trials, sample preparation, and analysis, besides being produced by an indigenously developed and patented technology, i.e., a cascaded membrane unit at the IICT laboratory in Hyderabad, India.

### *2.2. Methods*

#### *2.2.1. Synthesis of the nanofiltration membrane by the interfacial polymerization method*

The PES casting solution was prepared by dissolving 15 g of PES polymer powder in 85 mL of DMF solvent. The resulting bubble-free solution was cast onto a nonwoven polyester fabric support, fixed to a glass plate using a doctor blade. Immediately after casting, the glass plate with the fabric support was immersed in an ice-cold water bath (non-solvent) for 10 minutes to induce phase inversion and form a porous membrane. The resulting PES substrate was then immersed in a 2% aqueous piperazine (PIP) solution for 1 minute, followed by dip-coating in a hexane solution containing 0.2% trimesoyl chloride (TMC) for 30 seconds. The membrane was subsequently thermally cross-linked at 110 °C for 30 minutes, forming a thin polyamide (PA) selective layer. To obtain a PVA-coated PA membrane with a molecular weight cut-off (MWCO) of 300 Da (HF-NF-300 AR), the polyamide layer was hydrophilized by dipping the membrane in a 1.5 wt.% PVA solution, followed by thermal cross-linking at 120 °C for approximately 5 minutes. In this study, PIP served as the aqueous-phase diamine monomer, while TMC dissolved in hexane served as the organic-phase acyl chloride to form the selective polyamide layer via interfacial polymerization, as schematically illustrated in Fig. 1. The complete fabrication procedure of the HF-NF-300 AR membrane on the ultra-porous substrate using the interfacial polymerization method is shown schematically in the accompanying figure.

#### *2.2.2. Experimental set-up description for IPA purification by the Amicon cell filtration method*

The purification of IPA was carried out using an Amicon stirred cell fitted with a flat-sheet HF-NF 300AR depicted in Fig. 2. The membrane, with an active surface area of 0.0418 m² and a MWCO of 300 Da, was carefully placed on the membrane support inside the cell, ensuring that no air bubbles were trapped between the membrane and the support plate. Before each experiment, the membrane was pre-conditioned by rinsing with ultrapure water for 30 minutes to remove any residual preservatives and ensure complete wetting. A measured volume of 500 mL of LR grade IPA was then poured into the cell as the feed solution. The cell was sealed, and compressed nitrogen gas was introduced through a pressure line connected to the vessel's top. The operating pressure, initially set between 2–5 kg/cm², was gradually increased and maintained at 5.0 kg/cm², as monitored using an inline pressure gauge. To enhance mass transfer and minimize concentration polarization at the membrane surface, the integrated magnetic stirrer at the base of the cell was operated at a constant speed of 300 rpm throughout the experiment. Stirring ensured a homogeneous solute distribution and reduced the formation of a stagnant boundary layer, thereby improving permeate flux and metal ion

rejection. Filtration continued until the desired permeate volume was collected or the flux reached a steady state. The permeate was collected in pre-cleaned glassware, and samples from both permeate and retentate streams were taken for further analysis. These samples were analyzed using ICP-OES to determine trace metal concentrations and evaluate purification performance. After each run, the membrane was thoroughly cleaned with ultrapure water and stored in a 0.1% sodium metabisulfite (SMBS) solution to prevent microbial growth and scaling. The Amicon cell was also rinsed and dried before subsequent use.

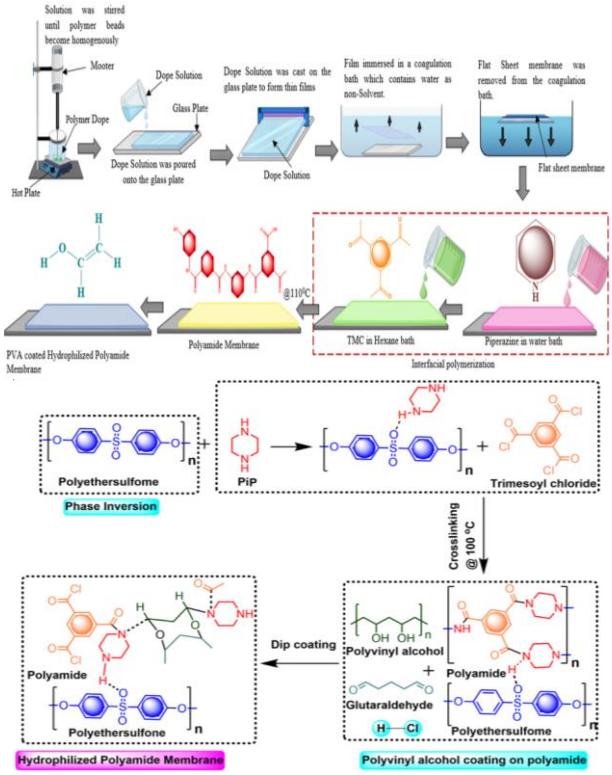


**Fig. 1.** Synthesis of the HF-NF-300 membrane by interfacial polymerization.

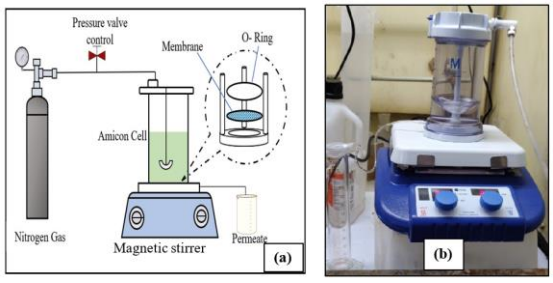


**Fig. 2.** a) Schematic diagram of the Amicon cell, b) Bench-scale lab experimental setup.

*2.2.3.Pilot plant studies of IPA using HF-NF 300 AR membrane:*

Based on the laboratory dead-end cell results, further experiments were performed in the pilot plant using the same membrane with an effective active surface area of 2.5 $m^2$. The entire experimental setup was placed inside the fume hood to prevent cross-contamination by following safety measures. Initially, 15 L of pre-measured IPA was charged to the feed tank and then pumped through the membrane using an air-operated diaphragm pump. The pressure in the membrane module was maintained at approximately 8 $kg/cm^2$ using the needle valve, and a complete set of experiments was conducted at this pressure. The reject flow rate was 180 LPH, and the permeate flow rate was 5 LPH. The average flux is around 2 L/m2.h, and the total permeate collected is 6.6 L. Recovery: 44%. Throughout the short-term pilot-scale experiments, no visible damage, delamination, or mechanical failure of the HF-NF-300 AR membrane or its PES support was observed, and post-run inspection confirmed that the module remained mechanically intact under IPA exposure.

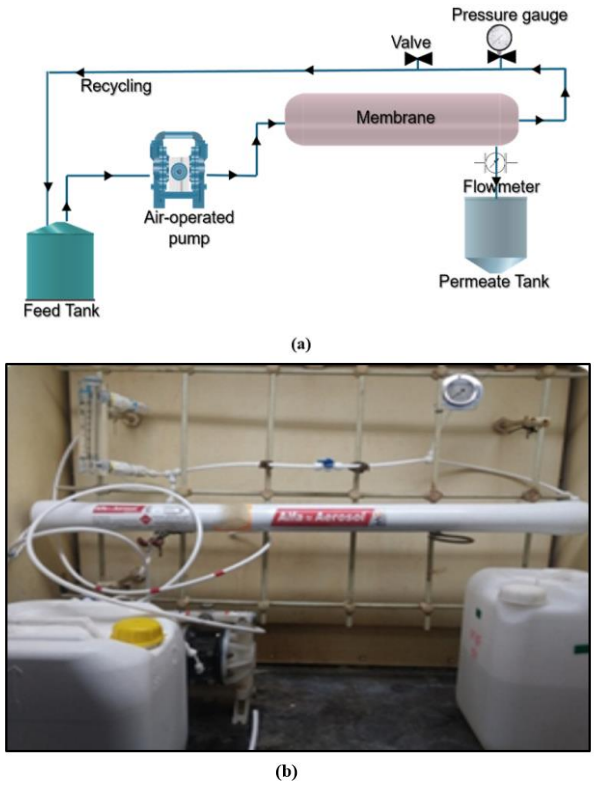


**Fig. 3.** a) Schematic of process flow diagram of pilot-scale experiment b) Pilot plant for IPA purification using HF-NF 300 AR membrane.

*2.2.4. Experimental set-up description for IPA purification by the vacuum distillation method*

A bench-scale vacuum distillation setup was utilized to purify LR-IPA. A 300 mL feed volume was added to a two-necked 500 mL round-bottom reboiler flask, which was then placed in a 300-watt electric heating mantle. The reboiler temperature was gradually increased using a mantle regulator to ensure controlled heating and prevent thermal shocks. As the temperature neared 90 °C, the feed began to vaporize under reduced pressure conditions. A vertical glass distillation column, with an internal diameter of 9.4 cm and a height of 37.6 cm, was connected to the reboiler. The system operated under a vacuum pressure of about 21.33 kPa (160 mmHg), with vapours evolving at a stable temperature of 85 °C. These vapours passed through the glass column and were then condensed in a coiled glass condenser with continuous chilled-water circulation. The condensed liquid was collected in a receiving flask, allowing for the separation of purified LR-IPA from impurities and residual components.

At this stage, the distillate was collected smoothly into a pre-cleaned receiver, with no noticeable fluctuations in vapour temperature or vacuum pressure, indicating that the system was operating at steady state. The distillation process lasted approximately 2 hours, during which 184 mL of purified isopropyl alcohol (IPA) was collected as distillate, while 110 mL of residue remained in the reboiler. To ensure a leak-proof operation, the entire setup was sealed using vacuum grease and PTFE gaskets. The pure IPA obtained under these steady-state conditions was preserved and subsequently analyzed for purity to assess the purification process's effectiveness. The results confirmed successful purification, revealing a significant reduction in impurities in the collected distillate compared to the initial feed.

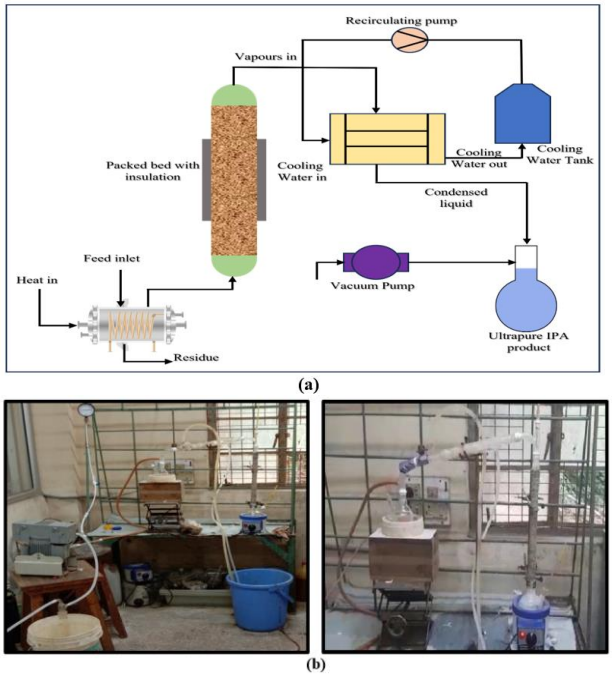


**Fig. 4**. a) Process Flow Diagram of Vacuum Distillation for IPA, b) vacuum distillation column set up for IPA purification

### *2.3. Simulation of Membrane Process*

#### *2.3.1 PRO-II Simulation Model Development*

The membrane properties derived from experimental findings, along with the thermodynamic relationships, can facilitate the execution of various case studies and optimization of membrane systems using commercial process simulation software. Aveva's PRO/II simulation tool can effectively model nanofiltration (NF) separation[14]. A customised membrane model was developed based on the Excel mixer example provided in the PRO/II software, and specific membrane configuration parameters were adopted from the research article [14]. A scientific approach using Excel unit operations to simulate a basic membrane system, as shown in Fig. 5, enables evaluation of performance and process optimization under varying operating conditions, including the number of membrane modules and feed pressure. By employing the Excel Unitop example from the simulator, a membrane model was constructed within the PRO/II flow sheet, which involved an Excel sheet designed to handle data from five feed streams, five products, ten integers, and twenty real parameters. The Excel unit operation within the simulator was employed to input the predicted flow rates and compositions for both the permeate and reject streams. The process model developed in PRO/II, along with its input file, was provided in the supporting information.

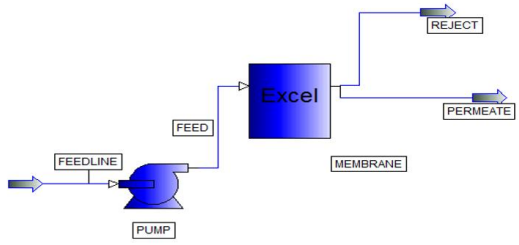


**Fig. 5.** PRO-II flow sheet used for simulation studies.

Performance evaluation and optimization potential were assessed by systematically adjusting the feed pressure with the help of pump. In addition to the feed pressure, the membrane area was varied during the simulation studies by increasing the number of membrane modules. Permeate pressure was maintained aligned to the experimental conditions. The supporting input file enabled estimation of the permeate flow rate, permeate concentration, and pump power requirements by varying the feed pressure and the number of membrane modules. The simulation results were subsequently used to calculate the product unit cost (PUC, $/m$^3$) using mathematical relationships derived from previous studies[14].

#### *2.3.2 Mathematical equations in PRO/II model*

In the present study, the solution-diffusion model was used, where the following equation defines the solvent flux:

$$J = \frac{\Delta V}{A \times \Delta t} = A_w \times \Delta P \tag{1}$$

where J is the solvent flux (L/m$^2$.h), $\Delta V$ is the permeate volume (L), $\Delta t$ is the filtration time (h), A is the effective area of the membrane in m$^2$, $A_w$ is the solvent permeability constant and ΔP is the hydraulic pressure gradient across the membrane.

The percentage of metal rejection is calculated by the following Eq. (2):

$$\%\text{Rejection} = (1 - \frac{Cp}{Cf}) \times 100 \tag{2}$$

$C_p$ and $C_f$ are the concentrations in permeate and feed, respectively.

The % recovery of the IPA was calculated using the following Eq. (3):

$$\%R = \frac{Qp}{Qf} \times 100 \tag{3}$$

where rejection is R, and the flow rates of feed and permeate are $Q_f$ and $Q_p$, respectively.

The metal ion flux equation is defined by the following equation[14]:

$$J_m = B_s \left( C_f - C_p \right) \tag{4}$$

$B_s$ is the metal ion permeability constant, while $C_f$ and $C_p$ are the feed and permeate concentrations.

The membrane unit was described using the solution–diffusion model for solvent and solute transport.

The solvent flux $J$ calculated as：

$$J = A_w \left( \Delta P - \Delta \pi \right) \tag{5}$$

where $A_w$ is the solvent permeability, $\Delta P$ is the transmembrane pressure, and $\Delta \pi$ is the osmotic pressure difference across the membrane.

For each stage, total and component mass balances were applied such that:

$$Q_f = Q_p + Q_r \text{ and } Q_f C_f = Q_p C_p + Q_r C_r \tag{6}$$

where $Q_f$, $Q_p$, and $Q_r$ denote the flow rates of feed, permeate, and retentate, and $C_r$ is the retentate concentration.

### *2.4. Membrane cleaning procedure*

Several research studies have shown that different cleaning methods are effective for removing metal ion deposits and other impurities from membrane surfaces. Chemical cleaning with reagents such as citric acid, sodium lauryl sulfate (SLS), sodium hydroxide (NaOH), EDTA, and sodium metabisulfite (SMBS) is beneficial. Among the physical, chemical, and biological cleaning approaches, chemical cleaning is the most commonly used because it is easy to apply and effective. The success of this method depends on the concentration, pH, and temperature of the cleaning solution. In this work, the NF membrane was first washed with an acid solution for about 30 minutes, followed by a 10-minute rinse with water. Then, it was cleaned with an alkaline solution for another 30 minutes, and again rinsed with water for 10 minutes. This two-step cleaning process helped remove both scales and organic matter from the membrane surface.

*2.5. Membrane characterization methods*

The synthesized membranes were thoroughly examined to assess their structural, morphological, and mechanical characteristics. Fourier-transform infrared spectroscopy (FTIR) and scanning electron microscopy (SEM) were used to identify chemical functionalities and examine the membrane surface features. FTIR spectra were recorded in the 400–4000 $cm^{-1}$ range using the KBr pellet technique (Nicolet-740, Perkin-Elmer-283B, Boston, MA, USA) to confirm the presence of characteristic functional groups in the polymer matrix. Surface and cross-sectional morphologies were observed using a field emission SEM (JEOL JSM-6500F, Japan) to evaluate the formation of the active layer and its interfacial integration with the support layer. Crystallinity and phase characteristics of the membranes were analyzed using X-ray diffraction (XRD, Siemens D5000) with a Cu Kα radiation source (λ = 1.54 Å) over a 2θ range of 2–80°. Thermal behaviour was examined by thermogravimetric and differential thermal analysis (TGA/DTA) using a Seiko 220 TG/DTA analyzer (Japan) under nitrogen flow (200 mL/min) from 25 to 800 °C at a heating rate of 10 °C $min^{-1}$. Mechanical strength and flexibility were evaluated by tensile testing (Instron Mini 44, USA), while surface wettability was determined using a VCA Optima contact angle goniometer (AST Products, USA). These combined analyses provided comprehensive insight into the physicochemical stability and mechanical performance of the synthesized membranes.

*2.6. Analytical instruments to measure the quantitative parameters*

The initial feed, permeate, and concentrate samples were analyzed using digital meters such as pH, conductivity, total dissolved solids (TDS), and turbidity. The acidity or alkalinity of an aqueous solution is expressed as pH, measured with a digital pH meter (DPH-500) purchased from Global Electronics, Hyderabad, India. Conductivity was measured from 0 to 200 mS/cm using a laboratory conductivity meter (DCM 900) procured from Global Electronics, Hyderabad, India. A Digital TDS meter (TDS-3, HM Digital, Hyderabad, India) was used to measure total dissolved solids, with a detection limit of 0-5000 ppm.

## 3. Results and discussion

*3.1. Membrane characterization*

*3.1.1. Morphology of membranes*

The surface and cross-sectional morphology of the HF-NF-300 membrane was examined using scanning electron microscopy (SEM), and the corresponding images are presented in Fig. 6. The membrane displays a typical asymmetric structure, characteristic of thin-film nanofiltration membranes. A dense, uniform selective top layer is clearly visible, serving as the primary barrier that rejects solutes while permitting solvent transport. This selective layer appears continuous and defect-free, confirming successful fabrication and the structural integrity of the active skin. The cross-sectional view (Fig. 6b) further reveals the smooth deposition of polyvinyl alcohol (PVA) over the dense polyamide (PA) layer, which penetrates the active porous polyethersulfone (PES) support and integrates seamlessly with the nonwoven polyethylene fabric base. The integrity of the PES support layer was evaluated qualitatively before and after IPA filtration using surface and cross-sectional SEM imaging; the post-filtration micrographs (Fig. 6c–d) do not show noticeable pore collapse, cracking, or delamination of the PES sublayer or the non-woven backing compared with the fresh membrane, indicating that the support maintains its morphology under the investigated IPA operating conditions. These observations indicate strong interfacial adhesion among the functional layers and effective PVA modification, both of which enhance wettability and operational stability. Beneath the selective layer, the substructure exhibits well-developed finger-like macrovoids interspersed with sponge-like regions extending throughout the membrane thickness. Such features reduce hydraulic resistance, promote higher flux, and provide mechanical reinforcement to the thin selective skin, while the hierarchical pore distribution mitigates compaction and minimizes internal concentration polarization, thereby supporting stable nanofiltration performance.

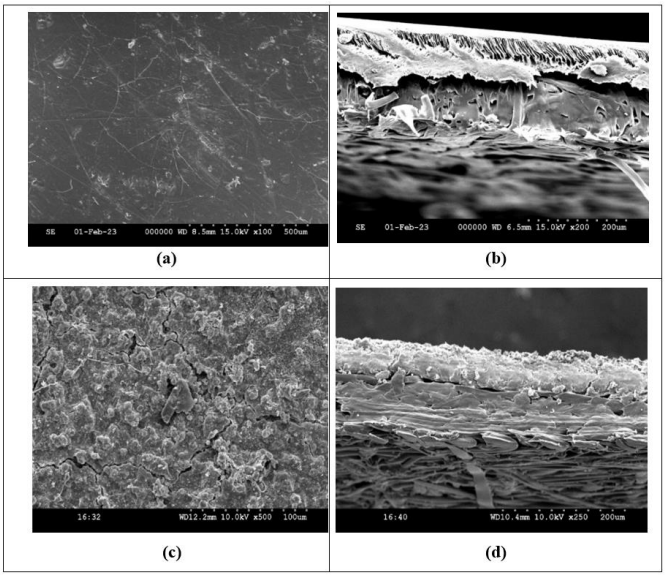


**Fig. 6.** a) Surface layer of membrane, b)cross section of HF-NF membrane, c)after IPA purification of NF membrane, and d) cross section of the NF membrane after purification.

*3.1.2. FTIR spectrum*

The FTIR spectrum of the HF-NF-300 membrane Fig. 7 confirmed the presence of key functional groups characteristic of thin-film nanofiltration membranes. Broad absorption bands at 3727 and 3376 $cm^{-1}$ correspond to –OH and –NH stretching vibrations, indicating surface hydroxyl groups and hydrogen-bonding interactions that enhance hydrophilicity. Peaks at 2924 and 2844 $cm^{-1}$ were attributed to $–CH_2$ stretching, reflecting the aliphatic backbone that contributes to mechanical stability. A strong band at 1644 $cm^{-1}$ indicated C=O stretching of polyamide or polyether urea linkages, confirming the formation of the selective active layer. Additional peaks at 1463 and 1371 $cm^{-1}$ corresponded to C–N stretching and $CH_2$ bending, while a band near 1150 $cm^{-1}$ was assigned to C–O–C stretching, suggesting the presence of ether linkages that improve flexibility and wettability. Sharp absorptions between 970 and 722 $cm^{-1}$ are attributed to aromatic and aliphatic bending vibrations, consistent with a crosslinked, heterogeneous composite structure. Overall, the FTIR results confirm that the HF-NF-300 membrane contains both hydrophilic (–OH, –NH, C=O, C–O–C) and hydrophobic ($–CH_2$, aromatic) groups. This balanced chemical composition enhances water permeability, solute rejection, and chemical robustness, making the membrane well-suited for solvent purification applications.

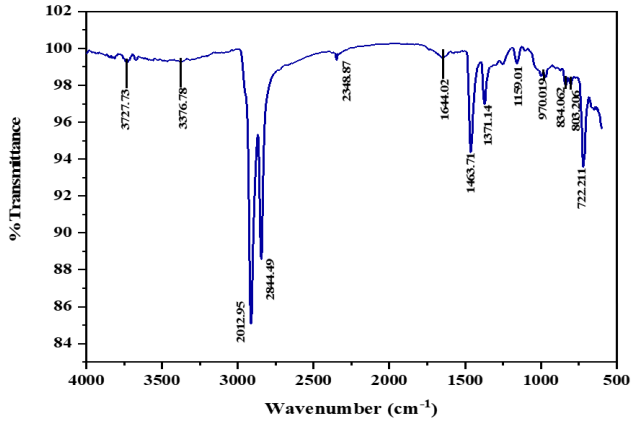


**Fig. 7.** FTIR spectra of HF-NF membrane.

*3.1.3. XRD*

The X-ray diffraction (XRD) pattern of the HF-NF composite membrane is shown in Fig. 8. The diffractogram confirms the semi-crystalline structure of the membrane, as evident from distinct peaks observed at 13.8°, 16.8°, 18.3°, 21.6°, and 24° on the 2θ scale. The presence of sharp reflections indicates ordered crystalline regions with a smaller d-spacing, which enhances ion sieving by selectively restricting the passage of divalent and multivalent ions. In contrast, the broader background peaks correspond to amorphous domains with larger inter-segmental spacing, which facilitate solvent transport and improve flux. The coexistence of crystalline and amorphous phases, therefore, provides a balance between selectivity and permeability. The membrane's layered structure also contributes to its separation performance. The polyamide (PA) selective layer, formed by interfacial polymerisation, governs IPA flux and rejection efficiency, while the underlying PES modification layer influences charge characteristics and cation selectivity. The synergistic effect of these layers enables effective rejection of metal ions present in IPA, without sacrificing permeability.

Furthermore, the semi-crystalline structure enhances the membrane's chemical and thermal stability under IPA exposure. The smooth surface morphology, combined with increased hydrophilicity, minimizes scaling and fouling tendencies while allowing easy recovery of performance after chemical cleaning. The XRD results confirm that the HF-NF composite membrane exhibits a semi-crystalline architecture that balances flux and rejection, making it well-suited for the purification of IPA.

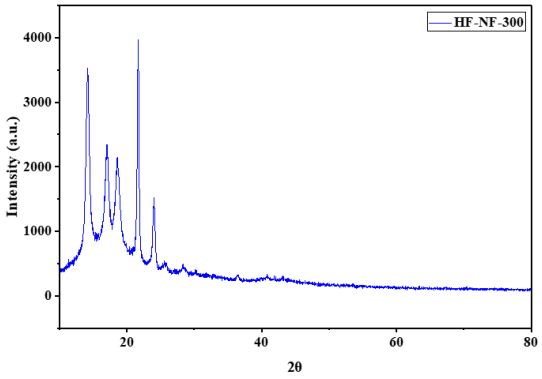


**Fig. 8.** XRD analysis of HF-NF 300 membrane.

*3.1.4. TGA*

The thermal stability of the HF-NF-300 AR membrane was evaluated under an inert nitrogen atmosphere, and the corresponding TGA profile is presented in Fig. 9. An initial gradual weight loss was observed up to approximately 250 °C, which can be attributed to the evaporation of physically adsorbed moisture. The release of residual volatile compounds entrapped within the polymer matrix. Beyond this stage, the membrane exhibited a pronounced weight reduction between 430 and 500 °C, corresponding to the thermal decomposition of the polymer backbone. This sharp decline is associated with the cleavage of hydroxyl and sulfone linkages, leading to chain scission and structural breakdown of the membrane material. The results indicate that the HF-NF-300 AR membrane maintains excellent thermal stability up to ~250 °C, which is well above the typical operating range for IPA purification processes. This robustness ensures structural integrity during solvent exposure and confirms its suitability for high-purity IPA recovery under industrial conditions.

*3.1.5. Tensile Strenth*

The mechanical strength of the HF-NF membrane was assessed through tensile testing and compared with that of a commercial cation-exchange membrane. At a crosshead speed of 5 mm/min, the HF-NF membrane exhibited a tensile strength of 32.48 MPa with an elongation at break of 20.74%. In contrast, the cation-exchange membrane showed a significantly lower tensile strength of 11.15 MPa but a higher elongation at break of 31.62%. These results suggest that while the HF-NF membrane is less flexible than the cation-exchange membrane, it offers considerably greater resistance to mechanical stress. The higher strength is attributed to the semi-crystalline polyamide layer and reinforced PES support, which provide robustness under pressurized IPA purification. Such mechanical stability is essential for sustained operation in both laboratory and pilot-scale systems, ensuring minimal deformation and long-term integrity during solvent filtration.

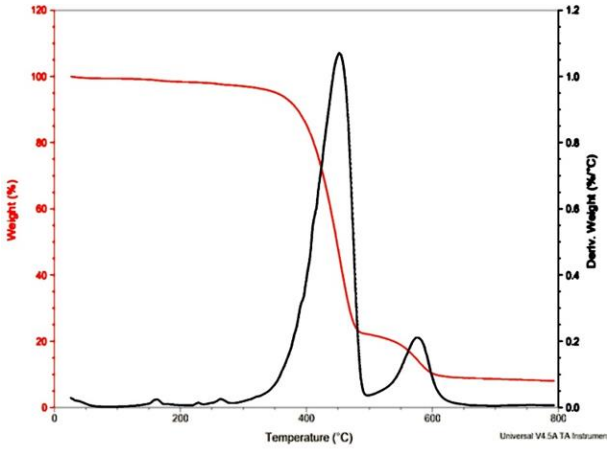


**Fig. 9.** TGA analysis of HF-NF-300 membrane.

*3.2 Experimental results*

The experiments were conducted in a dead-end metallic cell, an Amicon stirred cell NF process, and vacuum distillation for the purification of IPA. In each method, the metal removal from IPA and the membrane performance, in terms of permeate flux and recoveries, were calculated to assess the solvent's purity. After the membrane process, the obtained IPA permeate was further subjected to vacuum distillation to achieve higher metal rejection through fine-tuning. Therefore, the experimental results were calculated and reported by considering various flux and % metal-ion rejection parameters.

*3.2.1. Experimental study with an Amicon stirred cell*

*3.2.2. Effect of pressure on flux*

Fig. 10 illustrates the effect of membrane pressure on the flux performance of the NF membrane during IPA purification. As observed, the flux increases steadily and proportionally with applied pressure, ranging from 2.0 to 5.0 kg/cm². At the lowest pressure of 2.0 kg/cm², the membrane recorded a flux of 1.25 L/m²·h, indicating relatively low solvent permeation under minimal driving force. As the pressure was increased to 2.5 and 3.0 kg/cm², the flux improved to 1.89 and 2.28 L/m²·h, respectively, showing a positive pressure-dependent response. Beyond 3.0 kg/cm², the flux continued to rise more significantly, reaching 2.82 L/m²·h at 3.5 kg/cm², 3.43 L/m²·h at 4.5 kg/cm², and peaking at 4.11 L/m²·h under the highest tested pressure of 5.0 kg/cm².

This positive correlation between pressure and flux reflects typical behaviour in membrane filtration systems, where higher transmembrane pressure drives greater solvent flux. The curve shows a near-linear trend, suggesting that the membrane remains stable under increasing pressure, with no significant compaction or fouling in the tested range.

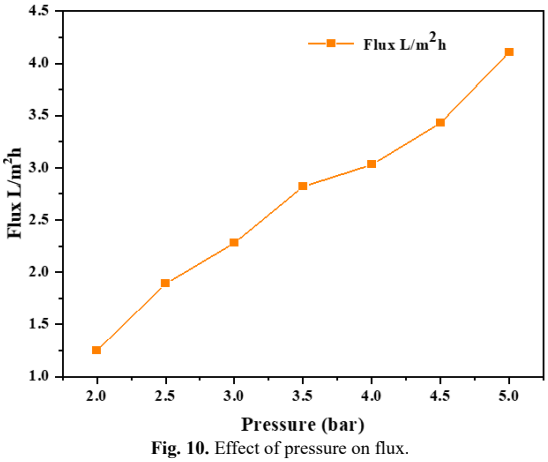


**Fig. 10.** Effect of pressure on flux.

*3.2.3. Effect of time on flux*

The membrane's permeation performance was evaluated using an Amicon cell with a feed volume of 500 mL at 5 bar operating pressure. A total permeate of 452 mL was collected over 70 minutes, corresponding to a total recovery of 90.4%. The overall average flux was calculated as 9.27 L/m².h, and the membrane exhibited a permeability of 1.85 L/m².h. Flux was observed to decline progressively over time, as shown in Fig.11. In the first 10 minutes, the flux reached 13.06 L/m²h, decreasing gradually to 5.02 L/m².h in the final interval of 70 min. This decline is characteristic of membrane operation and can be attributed to concentration polarization and partial fouling at the membrane surface.

The high initial flux indicates the membrane's intrinsic permeability under the given operating conditions, while the subsequent decline reflects the dynamic interplay between solute accumulation and membrane resistance over time. The interval-based flux analysis provides critical insight into the time-dependent performance of the membrane**,** highlighting the importance of monitoring short-term flux variations to optimize operational parameters and predict long-term membrane stability. These findings are consistent with typical observations in pressure-driven membrane processes, where initial high permeation rates gradually decrease as the system approaches equilibrium conditions.

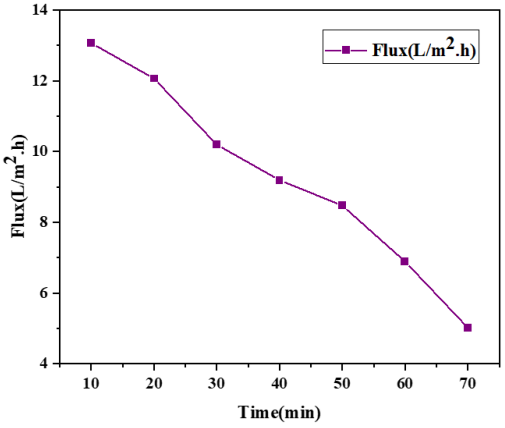


**Fig. 11.** Effect of time vs flux.

The HF-NF 300 demonstrated robust separation capability, with a high initial flux, and maintained adequate performance throughout the 70-minute experiment. These results support the suitability of HF-NF 300 membranes for separations requiring high recovery and consistent permeation.

*3.3. Experimental study on a pilot scale*

Pilot-scale studies play a crucial role in translating laboratory-scale findings into practical applications, providing realistic insights into the performance of membrane processes under operating conditions that closely mimic industrial environments. In this study, the HF-NF 300 membrane was selected due to its high selectivity, stability, and suitability for nanofiltration-based purification processes. Unlike bench-scale tests with limited feed volumes, pilot-scale experiments allow the evaluation of flux decline, recovery, and long-term operational stability, which are essential for process optimization and scale-up.

*3.3.1. Effect of pressure on flux*

The effect of applied pressure on permeate flux for the HF-NF-300 membrane is shown in Fig.12. At the lowest applied pressure of 4 bar, the membrane exhibited a flux of 1.32 L/m²·h, representing the baseline performance under minimal driving force. As the pressure increased to 5 bar, flux improved to 1.98 L/m²·h, and at 6 bar, it further increased to 2.78 L/m²·h. This sharp rise between 4 and 6 bar reflects the direct influence of transmembrane pressure on water transport, as the increased driving force overcomes the intrinsic resistance of the active layer, thereby facilitating greater permeation. Beyond 6 bar, however, the rate of flux improvement diminished noticeably. At 7 bar, the flux was 2.94 L/m²h, and at 8 bar, only a marginal increase to 3.01 L/m²h was observed. This near-stagnation indicates that the membrane is approaching a limiting flux region, where concentration polarization, fouling, and internal resistance reduce the effectiveness of additional pressure increments. In such conditions, additional energy input results in minimal productivity gain, making. Operation at higher pressures is inefficient. Overall, the results show that the HF-NF-300 membrane operates most efficiently at 5–6 bar, where flux enhancement is significant and proportional to the applied pressure. Beyond this point, the system transitions towards a resistance-limited regime, and the trade-off between flux gain and energy consumption becomes critical. The observed leveling-off of flux beyond 6 bar is mainly attributed to concentration polarization and increased boundary-layer resistance, which limit permeate transport despite further increases in applied pressure. Membrane compaction was negligible, as thickness measurements showed less than 0.3% variation at higher pressures.

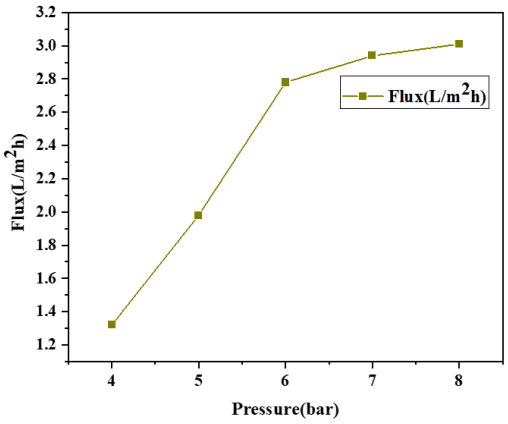


**Fig. 12.** Effect of pressure on flux.

*3.3.2. Effect of time on Flux*

The effect of operating time on permeate flux at an applied pressure of 8 bar is shown in Fig. 13. At the beginning of the experiment (15 min), the HF-NF-300 membrane exhibited a relatively high flux of 3.52 L/m²h. As the operation progressed, a gradual decline was observed. Flux decreased to 3.17 L/m²h at 30 min, 2.99 L/m²h at 45 min, and 2.64 L/m²h at 60 min. A more pronounced reduction occurred during extended operation, with values dropping to 2.29 L/m²h at 75 min and reaching only 1.23 L/m²h by 90 min. This corresponds to a flux loss of nearly 65% compared to the initial performance. The observed decline can be attributed to typical fouling phenomena and concentration polarisation. In the early phase (0–45 min), the reduction in flux is relatively moderate and can be attributed to rapid solute adsorption and partial pore blockage. Beyond 60 minutes, the sharper decline indicates the formation of a denser cake layer on the membrane surface, which imposes additional hydraulic resistance. At this stage, concentration polarization further increases solute accumulation near the membrane surface, thereby lowering the effective driving force across the active layer. The pronounced flux decay at extended operation times suggests the establishment of a limiting flux regime, in which additional transmembrane pressure does not translate into a proportional increase in flux due to mass transfer resistance. This phenomenon has been widely reported in nanofiltration studies and is indicative of the interplay between hydraulic resistance and solute accumulation at the membrane solution interface.

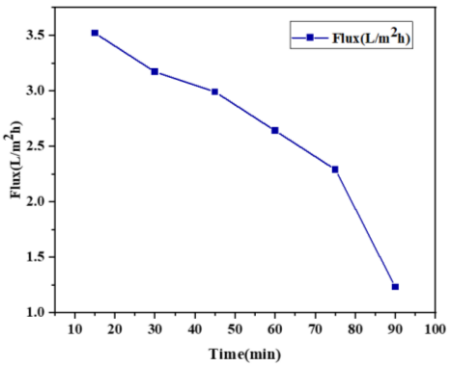


**Fig. 13**. Effect of time vs flux.

The pilot-scale experiments at 8 bar were conducted for 90 minutes and therefore represent short-term continuous operation rather than an actual long-term stability test. During this period, the permeate flux decreased by about 65% due to progressive fouling and concentration polarization, as shown in Fig. 13. However, after applying the chemical cleaning protocol described in Section 2.4, the pure IPA flux recovered to values close to the initial flux, indicating that the dominant resistance is reversible and that no significant irreversible degradation of the HF-NF-300 membrane in IPA occurred under the investigated conditions.

*3.3.3. Effect of time on flow rate*

At different feed pressures, the effect of operating time on permeate flow rate for the HF-NF-300 membrane is summarized in Fig. 14. Across all applied pressures (4–8 bar), permeate flow rate increased almost linearly with time, reflecting the progressive accumulation of permeate volume during extended operation. However, the rate of flow accumulation was strongly dependent on the applied transmembrane pressure. At 15 minutes, the permeate flow rate ranged from 0.713 L/h at 4 bar to 1.375 L/h at 8 bar, while at 60 minutes these values rose to 2.85 L/h and 5.50 L/h, respectively. By 150 minutes, the permeate flow rate reached 7.125 L/h at 4 bar and 13.75 L/h at 8 bar, demonstrating a clear enhancement in water permeability with increasing applied pressure. Notably, the permeate flow rate at pressures ≥7 bar was markedly steeper than at pressures ≤5 bar, indicating more efficient permeation under a stronger driving force. The results further suggest that although operation at 7–8 bar yields higher instantaneous flow rates, the marginal benefit must be weighed against the potential for accelerated fouling, increased energy demand, and reduced long-term membrane stability. Conversely, intermediate pressures (5–6 bar) offer a more balanced performance, with substantial permeate generation and comparatively lower risk of rapid fouling kinetics.

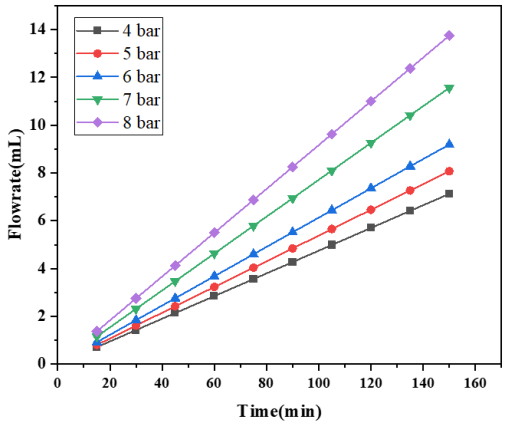


**Fig. 14**. Effect of time on permeate flow rate.

Overall, the pressure-dependent permeate flow rate profiles confirm that transmembrane pressure is a dominant operational variable in governing NF membrane productivity. However, operation beyond the optimal pressure range risks diminishing returns due to fouling-related resistance, underscoring the importance of selecting conditions that balance permeate yield, recovery, and system sustainability.

*3.4 Purity levels of trace metal ions in IPA % rejection from experimental studies.*

The rejection performance of different purification processes for the removal of metallic ions from IPA was evaluated using laboratory-scale Amicon cell filtration, pilot-scale membrane experiments, and conventional distillation (shown in Fig. 15). The results are summarized in Table 1. The Amicon cell experiments demonstrated an average rejection of 91.97%, indicating that membrane-based nanofiltration is effective in retaining most metal ions under controlled small-scale conditions. High rejection efficiencies were observed for divalent and multivalent cations such as Ba (99.5%), Mg (99.31%), Mn (99.14%), and Ag (99.25%), while relatively lower values were obtained for metalloids such as As (64.83%) and alkali metals like K (85%) and Na (98.43%). These results confirm that nanofiltration is highly selective towards multivalent ions, though less effective for smaller monovalent cations and metalloids due to their higher diffusivity and weaker interaction with the membrane surface.

In the pilot-scale system, the overall rejection averaged 95.43%, with most ions showing consistent removal of ~82–83%. The relatively uniform rejection values across different ions suggest that scale-up introduces hydrodynamic and operational complexities, such as concentration polarization and reduced effective retention, which diminish the selectivity observed in small-scale Amicon cell tests. Nevertheless, the performance remained satisfactory for preliminary purification, establishing the feasibility of scaling membrane operations for industrial IPA processing. After a pilot-scale experiment followed by vacuum distillation, the highest level of purification is achieved, with an average rejection of ~97.3%. Distillation exhibited the highest overall rejection, and achieved near-complete removal for several ions, including Ca (99.9%), Na (99.57%), Cr (99.53%), and Mg (99.46%). The lowest rejection rates were observed for Ni (93.36%) and Sr (93.96%), which still exceeded 93%. This confirms that distillation is highly effective in removing a broad spectrum of metal ions, surpassing both laboratory and pilot-scale membrane processes. However, its higher energy consumption compared to membranes must be considered in process optimization. Integrated hybrid purification delivers ultrapure IPA suitable for semiconductor manufacturing applications. While distillation remains the most effective approach for achieving ultra-low metal ion concentrations, membrane-based purification, particularly at pilot scale, offers a more energy-efficient and scalable pathway, especially when combined with downstream distillation polishing.

**Table 1**
Trace Metal ion ICP-OES analysis of % rejection of IPA.

| Trace metals | Units= ppb (nano g/mL) | | | | | | | | |
|---|---|---|---|---|---|---|---|---|---|
| | Desired Spec for SEMI grades | ICP-OES and GFAAS analyses | | | | | | | |
| | | IPA LR Grade Feed | Amicon Permeate (ppb) | Amicon % Rejection | Pilot-scale Permeate (ppb) | Pilotscale % Rejection | Distillation Permeate (ppb) | Distillation % Rejection | LOD |
| Ag | 0.1 | <13 | 0.20 | 98.46 | 2.30 | 82.31 | 0.10 | 99.23 | 0.2 |
| Al | 0.1 | <80 | 0.60 | 99.25 | 14.15 | 82.31 | 0.40 | 99.5 | 0.6 |
| Ca | 0.2 | 96 | 33.76 | 64.83 | 17.01 | 82.31 | 5.34 | 94.44 | 1 |
| Cd | 0.1 | 20 | 3.54 | 82.29 | 3.54 | 82.31 | 1.03 | 94.83 | 0.1 |
| Co | 0.1 | 43 | 0.22 | 99.5 | 7.61 | 82.31 | 1.82 | 95.76 | 0.7 |
| Cr | 0.1 | 27 | 0.44 | 98.37 | 4.78 | 82.31 | 0.03 | 99.9 | 0.3 |
| Cu | 0.1 | <21 | 1.56 | 92.59 | 3.72 | 82.31 | 0.23 | 98.91 | 0.2 |
| Fe | 0.3 | <7 | 0.67 | 90.43 | 1.24 | 82.31 | 0.03 | 99.53 | 0.4 |
| Li | 0.1 | 7 | 0.08 | 98.87 | 1.24 | 82.31 | 0.05 | 99.26 | 0.3 |
| Mg | 0.1 | 37 | 1.59 | 95.71 | 6.55 | 82.31 | 0.83 | 97.76 | 0.2 |
| Mn | 0.1 | <2 | 0.32 | 83.78 | 0.35 | 82.31 | 0.06 | 97.14 | 0.3 |
| Na | 0.2 | 446 | 66.90 | 85 | 78.91 | 82.31 | 24.34 | 94.54 | 0.1 |
| Ni | 0.1 | 44 | 2.27 | 94.84 | 7.78 | 82.31 | 1.26 | 97.14 | 0.3 |
| Pb | 0.1 | <70 | 0.48 | 99.31 | 12.38 | 82.31 | 0.38 | 99.46 | 0.6 |
| Zn | 0.1 | 157 | 1.35 | 99.14 | 27.78 | 82.31 | 2.13 | 98.64 | 0.1 |

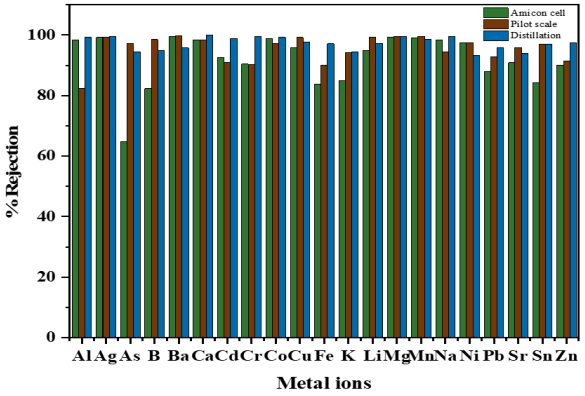


**Fig. 15.** Trace metal ion % rejection.

### *3.5. Simulation of the membrane process*

As a membrane system designer, the primary objective is to maximize permeate purity while minimizing the overall membrane area and energy consumption. In this work, PRO-II simulations were conducted for the purification of IPA, targeting a product flow rate of 520 $m^3$/day at feed pressures of 8–20 bar. The number of membrane modules ranged from 1 to 30, with each module having an effective membrane area of 37.2 $m^2$. The simulation outputs, including pump power, permeate flow rate, and permeate concentration, were analyzed to evaluate three critical performance indicators: product unit cost (PUC), flux, and rejection.

Various case study results obtained with membrane feed pressures in the range of 8-20 bar, a permeate flow rate of 3.824 m3/h, and different numbers of membrane modules were exported from PRO-II into Excel for further analysis. Subsequently, the membrane performance parameters Product Unit Cost (PUC), flux, and rejection were computed, and the results were presented graphically in Fig. 16.

The variation of PUC with membrane feed pressure is shown in Fig. 16(a). As seen in the results, PUC increased linearly with pressure, rising from 2.75 \$/$m^3$ at 8 bar to 187.87 \$/$m^3$ at 35 bar. As the simulation was carried out at a fixed flow rate of 520 $m^3$/day, the operating cost of the process was pump power and remained the same at any given feed pressure, irrespective of the number of membrane modules. However, at the specified feed pressure, as the number of modules in the simulation increased from 1 to 35, the membrane's fixed cost increased. Overall, as the PUC is growing linearly, this analysis alone cannot be used to determine the optimum, and it needs to be correlated with flux and rejection, as explained subsequently.

Solvent flux variation with the module count at different membrane feed pressures is shown in Fig.16(b). From the results, it is observed that the flux does not change significantly with pressure at low membrane area, and it is in the range of 11-11.25 $m^3/m^2$.h. Flux increased with increasing membrane area from 1 module to 35 modules. However, at a high membrane area of 30 modules, the flux varied between 200 and 289.95 $m^3/m^2$.h, with pressure ranging from 8 to 30 bar. The nearly linear increase with both module number and pressure reflects the proportional rise in available membrane surface area and driving force. The absence of non-linear deviations indicates that no significant mass-transfer limitations occurred under the tested operating conditions, and the system can be expanded effectively without compromising flux performance.

Rejection behaviour is illustrated in Fig.16(c). From the results, it was observed that at the lowest membrane feed pressure of 8 bar, rejection improved from 87% to 97% as the membrane area increased from 1 module to 35 modules. Rejection reached 95% with 10 modules, and then the improvement in rejection slowed with further increases in the area, reaching 97% with 35 modules. Similar trends were observed at higher pressures, where rejection consistently surpassed 98.2% beyond 15 modules. These results confirm that the membrane system maintains stable and robust rejection performance across a wide operating window, ensuring the removal of both ionic and organic impurities to meet semiconductor-grade IPA specifications.

Considering the product unit cost, solvent flux, and rejection together, the optimum operating window at 20 bar pressure with 10-15 membrane modules to achieve an acceptable flux of 150 L/m2.h and 98.2% rejection, leading to a PUC of 100 \$/$m^3$. Overall, the findings confirm that membrane-based IPA purification can be effectively optimized through PRO-II simulation, and that careful adjustment of pressure and module configuration is essential to achieve cost-effective, ultrapure IPA suitable for semiconductor and pharmaceutical applications.

Based on this analysis, operating at 20 bar with 15 modules provides the most practical balance of purity, scalability, and cost efficiency, making it the recommended configuration for industrial-scale IPA purification.

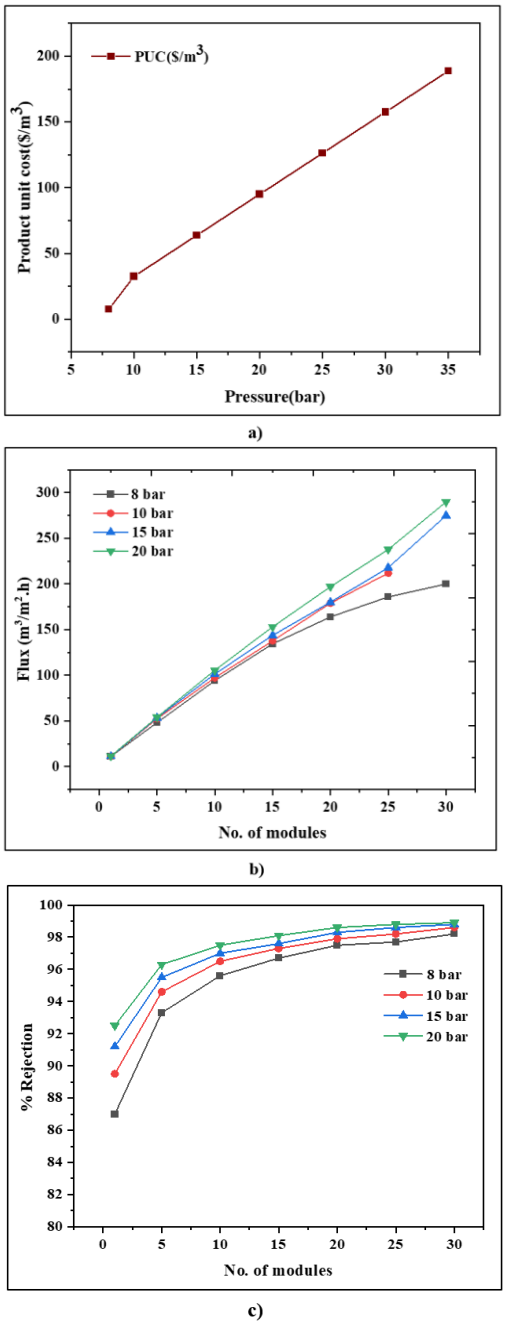


**Fig. 16:** a) Effect of No.of modules vs PUC(\$), b) Effect of no. of modules vs flux, and c) Effect of Pressure vs % rejection.

**Table 2**
Comparison of current work with literature for IPA purification.

| S.No | Method &Setup | Key Findings | Reference |
|---|---|---|---|
| 1 | Nanofiltration (Dow NF270, poly(piperazine-amide)) on water–alcohol mixtures (MeOH, EtOH, IPA) up to ≈30 vol% alcohol | Permeate flux decreased with increasing alcohol fraction; membrane swelling, viscosity, and dielectric changes affected transport and polarization. | [15] |
| 2 | Pervaporation with commercial CMC-CF-23 membrane on pharmaceutical effluent (~17% IPA + water + HCl/NaCl) | Reduced water from ~35 wt% (feed) to ~0.3 wt% (product); flux increased with temperature (50–80 °C); demonstrated industrial effluent treatment by PV. | [16] |
| 3 | Pervaporation using PVA modified by Pluronic F127 on PA substrate; IPA–water feeds (12–80 wt% water) | Permeation flux 0.100–1.164 $kg \cdot m^{-2} \cdot h^{-1}$; permeate water content 84.6–98.8 wt% depending on feed/composition and membrane design. | [17] |
| 4 | FAU-type zeolite membrane — vapour permeation/pervaporation for IPA–water dehydration | High water permselectivity and permeance; FAU showed better stability than LTA in high-water feeds. | [3] |
| 5 | Vacuum membrane distillation (VMD) using hollow-fiber / capillary modules (lab scale); ethanol and winery effluents used as test feeds | Demonstrated concentration factors (4–6.5× continuous), validated model with experimental data; explored module & operating impact on flux/concentration. | [18] |
| 6 | Vacuum membrane distillation (VMD) for IPA recovery; polypropylene hollow-fiber membranes; data-driven (Bayesian) optimization of operating parameters (lab scale) | Demonstrated optimized VMD conditions for IPA recovery from wastewater; showed how VMD parameters (temp, vacuum, flow) affect recovery and long-term stability | [19] |
| 7 | NF (Amicon bench + pilot 2.5 $m^2$) + vacuum distillation + PRO-II simulation | ~91–95% rejection (NF); ~97.3% rejection (NF + distillation); >98.2% predicted rejection (simulation); scalable to 520 $m^3$/day | **Present study** |

## 4. Conclusions

This study demonstrates the effectiveness of a hybrid nanofiltration–distillation strategy for producing ultrapure IPA suitable for semiconductor applications. Laboratory-scale experiments with the HF-NF-300 membrane achieved 91–95% rejection of metal ions while maintaining stable flux. Pilot-scale trials with a 2.5 $m^2$ HF-NF-300 module confirmed the process's scalability, demonstrating consistent separation performance. Distillation polishing of pilot scale permeates further enhanced purity, achieving ~97.3% overall rejection of contaminants. PRO-II simulation validated the feasibility of scaling this hybrid system to an industrial capacity of 520 $m^3$/day, with predicted rejection levels exceeding 98.2%. The integration of NF and distillation addresses the limitations of conventional purification methods by combining selective ion removal with efficient separation of volatile impurities. The synergy between experimental validation and process simulation ensures both technical feasibility and industrial scalability. Overall, this hybrid nanofiltration–distillation process provides a reliable, energy-efficient, and sustainable route for the large-scale production of ultrapure IPA, meeting the stringent purity requirements of the semiconductor industry.

## Credit authorship contribution

*D. K. Fothedar:* Conceptualization, Data curation, Formal analysis, Visualization, Writing original draft.
*N. Sahu*: Writing-review & editing.
*N. R. Choudhury*: Supervision, Validation.
*S. Sridhar:* Supervision, Correction, Validation.

## Declaration of Competing Interest

The authors declare that they have no known competing financial interests or personal relationships that could have appeared to influence the work reported in this paper.

## Data availability

Data will be made available on request.

## Acknowledgement

The author of the manuscript acknowledges the AcSIR, Ghaziabad, India, and the CSIR, New Delhi, India, for providing a senior research fellowship to support the PhD work. This work was performed under the GAP-713 project. This article's communication number is **IICT/Pubs./2025/374.**

## References

[1] I.-K. Lee and B.-D. Choi, "A Study on the Role of Pre-Cleaning and a New Method to Strengthen Gate Oxide Quality," Nanomaterials, vol. 12, no. 9, p. 1563, May 2022, https://doi.org/10.3390/nano12091563.
[2] S. Lin, "Recovery of isopropyl alcohol from waste solvent of a semiconductor plant," J. Hazard. Mater., vol. 106, no. 2–3, pp. 161–168, Jan. 2004, https://doi.org/10.1016/j.jhazmat.2003.11.012.
[3] T. V. N. Nguyen, L. Paugam, P. Rabiller, and M. Rabiller-Baudry, "Study of transfer of alcohol (methanol, ethanol, isopropanol) during nanofiltration in water/alcohol mixtures," J. Memb. Sci., vol. 601, p. 117907, Mar. 2020, https://doi.org/10.1016/j.memsci.2020.117907.
[4] P. Rostam-Khani, M. J. P. Hopstaken, P. Vullings, G. Noij, O. O'Halloran, and W. Claassen, "Quantification issues of trace metal contaminants on silicon wafers by means of TOF-SIMS, ICP-MS, and TXRF," Appl. Surf. Sci., vol. 231–232, pp. 720–724, Jun. 2004, https://doi.org/10.1016/j.apsusc.2004.03.030.
[5] J. Park, M. Cheon, S. Park, J. H. Lee, and D.-Y. Koh, "Sustainable Isopropyl Alcohol Recovery via Data-Driven, Active-Learning Optimization of Vacuum Membrane Distillation," ACS Sustain. Chem. Eng., vol. 12, no. 31, pp. 11510–11519, Aug. 2024, https://doi.org/10.1021/acssuschemeng.4c01285.
[6] P. V. Buragohain, W. N. Gill, and S. M. Cramer, "Novel Resin-Based Ultrapurification System for Reprocessing IPA in the Semiconductor Industry," Ind. Eng. Chem. Res., vol. 35, no. 9, pp. 3149–3154, Jan. 1996, https://doi.org/10.1021/ie960017j.
[7] M. Quillen, P. Holbrook, and J. Moore, "Optimizing surface finishing processes through the use of novel solvents and systems," Mar. 2007, p. 651841, https://doi.org/10.1117/12.713407.
[8] K. Asada et al., "A new economical wafer drying technology with high process performance," in 1997 IEEE International Symposium on Semiconductor Manufacturing Conference Proceedings (Cat. No.97CH36023), pp. E13–E16, https://doi.org/10.1109/ISSM.1997.664555.
[9] B. . Van Baelen, G., Vreysen, S., Gerbaud, V., Rodriguez-Donis, I., Geens, J., & Janssens, "Isopropyl alcohol recovery by heteroazeotropic batch distillation."
[10] A. Lee, A. Naquash, M. Lee, Y. D. Chaniago, and H. Lim, "Exploitation of distillation for energy-ef fi cient and cost-effective environmentally benign process of waste solvents recovery from semiconductor industry," Sci. Total Environ.
[11] W. Z. A. W. Jusoh, S. A. Rahman, A. L. Ahmad, and N. M. Mokhtar, "Modifications on Polymeric Membranes for Isopropanol Dehydration Using Pervaporation: A Review," 2020, pp. 97–124.
[12] B. Liang, X. He, J. Hou, L. Li, and Z. Tang, "Membrane Separation in Organic Liquid: Technologies, Achievements, and Opportunities," Adv. Mater., vol. 31, no. 45, Nov. 2019, https://doi.org/10.1002/adma.201806090.
[13] Y. XING, B. SU, and H. ZHEN, "Research Progress of Solvent-Resistant Nano-Filtration Membranes," https://doi.org/10.11949/0438-1157.20200792.
[14] R. Kancherla, R. K. Vadeghar, P. R. Ginuga, and S. Sridhar, "Antifouling membrane based on sodium alginate coated polyamide thin film composite

for desalination of brackish water," Polym. Eng. Sci., vol. 60, no. 11, pp. 2827–2840, 2020, https://doi.org/10.1002/pen.25515.

[15] P. Marchetti, L. Peeva, and A. Livingston, "The Selectivity Challenge in Organic Solvent Nanofiltration: Membrane and Process Solutions," Annu. Rev. Chem. Biomol. Eng., vol. 8, no. 1, pp. 473–497, Jun. 2017, https://doi.org/10.1146/annurev-chembioeng-060816-101325.

[16] M. Galizia and K. P. Bye, "Advances in Organic Solvent Nanofiltration Rely on Physical Chemistry and Polymer Chemistry," Front. Chem., vol. 6, Oct. 2018, https://doi.org/10.3389/fchem.2018.00511.

[17] A. Rastegar et al., "Particle control challenges in process chemicals and ultra-pure water for sub-10nm technology nodes," Apr. 2014, p. 90480P, https://doi.org/10.1117/12.2048080.

[18] A. M. Urtiaga, E. D. Gorri, and I. Ortiz, "Pervaporative recovery of isopropanol from industrial effluents," Sep. Purif. Technol., vol. 49, no. 3, pp. 245–252, May 2006, https://doi.org/10.1016/j.seppur.2005.10.006.

[19] M. Dmitrenko, R. Atta, A. Zolotarev, A. Kuzminova, S. Ermakov, and A. Penkova, "Development of Novel Membranes Based on Polyvinyl Alcohol Modified by Pluronic F127 for Pervaporation Dehydration of Isopropanol," Sustainability, vol. 14, no. 6, p. 3561, Mar. 2022, https://doi.org/10.3390/su14063561.